

Modeling of Antimortar Lethality by a Solid-State Heat-Capacity Laser

C. D. Boley* and A. M. Rubenchik¹

Lawrence Livermore National Laboratory, University of California,
Livermore, California 94551

We have studied the use of a solid-state heat-capacity laser (SSHCL) in mortar defense. This type of laser, as built at Lawrence Livermore National Laboratory, produces high-energy pulses with a wavelength of about 1 μm and a pulse repetition rate of 200 Hz. Currently, the average power is about 26 kW. Our model of target interactions includes optical absorption, two-dimensional heat transport in the metal casing and explosive, melting, wind effects (cooling and melt removal), high-explosive (HE) reactions, and mortar rotation. The simulations continue until HE initiation is reached. We first calculate the initiation time for a range of powers on target and spot sizes. Then we consider an engagement geometry in which a mortar is fired at an asset defended by a 100-kW SSHCL. Propagation effects such as diffraction, turbulent broadening, scattering, and absorption are calculated along the trajectory, by means of a validated model. We obtain kill times and fluences, as functions of the rotation rate. These appear quite feasible.

KEYWORDS: Engagement scenario, High explosive, Lethality, Mortar, Solid-state laser

Nomenclature

| | |
|----------|---|
| C | specific heat |
| C_n^2 | refractive index structure constant |
| D | thermal diffusivity |
| E | high-explosive activation energy |
| F | fluence |
| h | slab thickness |
| I | laser intensity |
| k | Boltzmann factor |
| P | laser power |
| Q | heat of decomposition |
| T | temperature |
| Z | preexponential factor (high-explosive kinetics) |
| α | optical absorptivity |
| κ | thermal conductivity |
| ρ | density |

Received November 10, 2005; revision received June 6, 2006.

*Corresponding author; e-mail: boley1@llnl.gov.

¹E-mail: rubenchik1@llnl.gov.

1. Introduction

Our laboratory and industrial collaborators have been developing solid-state heat-capacity lasers (SSHCLs) since 1997. These devices represent a new concept in tactical battlefield weapons, in that heat-capacity operation provides a compact and mobile laser architecture suitable for scaling to powers relevant to engagements. The lasers produce bursts of pulses, while the waste heat is stored in the medium (solid-state slabs). After sufficient heating, the hot slabs are switched out for rapid cooling while cool slabs are simultaneously switched into the aperture. The lasers are designed for flexible platform requirements. Until recently, the most powerful such laser [also built at Lawrence Livermore National Laboratory (LLNL)] contained nine Nd:glass slabs pumped by flashlamps. It produced a power of 10 kW (500 J/pulse with a pulse repetition rate of 20 Hz), at a wavelength of 1.053 μm . The material interactions of this laser and a predecessor have been studied at some length.¹⁻³ Excellent beam quality has been demonstrated.¹⁰ The most recently built SSHCL¹² has four ceramic YAG slabs pumped by diodes at 200 Hz. The pulse length is about 0.5 ms. Routine operation at a time-averaged power of about 26 kW (130 J/pulse) for several seconds has been achieved.

We are concerned here with a future battlefield configuration of this last laser, upgraded in power to 100 kW. We evaluate its lethality in an engagement with an M252-type mortar. The analysis proceeds in two steps: 1) calculation of target interactions, including ignition of the high explosive (HE), over a range of powers on target and spot sizes; and 2) calculations of propagation and engagement for a mortar trajectory, using the results of the first step.

Other prominent lethality and engagement studies performed in the past several years include those of Kulkarny et al.⁹ and Nugent et al.,¹¹ which involved different choices of lasers and targets. An overview of pulsed laser lethality, including material removal, was given by Wenzel.¹³ Historically, studies of the interactions between a laser beam and HE date back at least to the 1970s.⁸

2. Target Interactions

For our purposes, we model an M252 mortar as a cylinder of diameter 8 cm, consisting of an iron casing of thickness 1 cm, filled with trinitrotoluene (TNT). We neglect the tapering of the vessel and variations in the casing thickness. The chosen value is conservative. Mortars are aerodynamically stabilized with fins, but various imperfections may give rise to a rotation rate nearing 10 rpm. In our scenarios, the mortar is killed via rapid cook-off of the HE. During this process, the beam directly heats the steel container, raising the temperature of the adjacent HE to initiation. At this moment, only a fraction (or possibly none) of the container width has been melted. Thus the reaction products are confined, increasing the pressure and stimulating the HE explosion and mortar destruction.

The main physical processes in the target are absorption of the incident laser energy by the metal, heat conduction in the metal and explosive, and reaction kinetics in the explosive. The wind also plays a role by removing melt and cooling the surface. The geometry is depicted in Fig. 1. We have developed a computational model (THALES), which simulates these processes throughout the engagement until the moment of HE initiation. Calculations are performed in two-dimensional (r, z) symmetry. The model employs a database of material properties, such as the heat capacity, the thermal conductivity, and the absorptivity. An important feature of these properties is their temperature dependence, which can be pronounced.

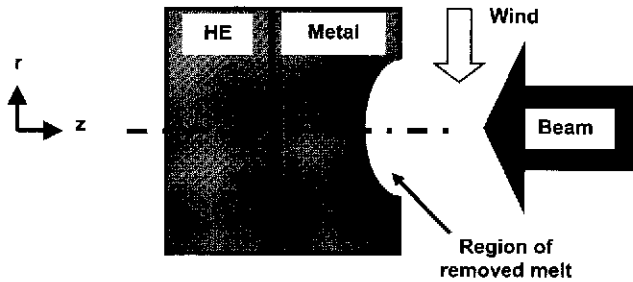


Fig. 1. Geometry of the target interaction model.

In the application to mortars, we supplement this model with HE reactions. These are described by Arrhenius kinetics,^{6,14} occurring in the temperature equation according to

$$\rho C \frac{\partial T}{\partial t} = \nabla \cdot \kappa \nabla T + \rho Q Z \exp(-E/kT). \quad (1)$$

The first term on the right-hand side describes heat conduction, while the second term describes HE reactions. The driving laser absorption occurs as a boundary condition involving the surface absorptivity of the metal. The quantities Q , E , and Z are, respectively, the heat of decomposition, the activation energy, and a characteristic reaction rate (“preexponential factor”). Their values, as inferred from experiments with HE, are quite reliable. The exponential term leads to extremely rapid heating once initiation is reached. Vapor generation and disassembly, which are outside the scope of the model, then take place. Our simulations terminate when the temperature anywhere within the HE (in practice, near the interface with the metal, on the beam axis) suddenly spikes. The temperature at which this occurs depends on the spot size and the rate of heating. It is about 550–600°C in our simulations. This decreases for larger spots and lower heating rates.

In the interval between pulses (about 4.5 ms), heat diffuses a short distance in the target. This is of order $(4Dt)^{1/2} \sim 0.04$ cm, in which an approximate thermal diffusivity of $0.1 \text{ cm}^2/\text{s}$ has been used. This length is small compared to typical target dimensions. As a result, the macroscopic heat distribution is governed by the time-averaged power deposition. Thus the pulsed beam format can be simulated by a continuous-wave (CW) format having the same time-averaged power. Note that a pulse repetition rate of 200 Hz, with pulses of duration 0.5 ms, corresponds to a duty factor of 10%. Consequently, an individual pulse carries 10 times the power of an equivalent CW beam. The absorptivity of metals typically increases with temperature. Since a pulsed beam produces somewhat higher peak surface temperatures than a CW beam of the same average power, it also produces somewhat higher energy deposition. This difference, however, decreases as the duty factor increases. Our simulations show little difference for a 10% duty factor. In addition, the increase of absorptivity with temperature is small for the target casing material considered here.

At the target, we assume a Gaussian radial beam profile. Therefore the intensity has the form $I(r) = (P/\pi a^2) \exp(-r^2/a^2)$, in terms of the time-averaged power P on target and the $1/e$ spot radius a .

In our model, melt is assumed to be removed by the wind. In the Eulerian zone scheme of the model, this means that a particular zone is removed when its temperature reaches the melting temperature. Physically, the melted material is a nearly incompressible liquid, with a low kinematic viscosity, comparable to that of water. Airflow sets up tangential stresses

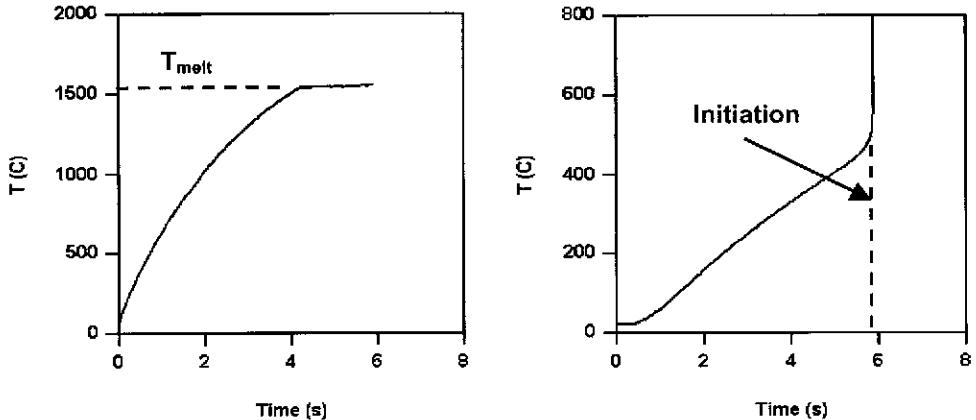


Fig. 2. Simulation of 30-kW beam on 1-cm-thickness iron, shielding TNT (beam $1/e$ radius of 2.5 cm). Left: temperature of front edge of iron, on axis. Right: maximum temperature in HE.

that result in rapid removal of all the melt except for a thin layer. Estimates indicate that the thickness of this layer (tens of microns) is small compared with scales of physical interest. Wind cooling is also included. In the simulations, the assumed wind speed is Mach 0.3. The simulations are insensitive to the precise speed, since wind cooling is not a major effect in our regime and melt removal occurs independently of the wind speed.

As an example, let us first consider a 30-kW beam on target, with $1/e$ spot radius 2.5 cm, and assume that the target is not rotating. As shown in Fig. 2, the temperature of the front edge, on the beam axis, rises to the melting temperature ($\sim 1,540^\circ\text{C}$) within about 4 s. It remains clamped at this level, as melt is removed by the wind. The maximum temperature in the HE rises steadily until, at about 5.9 s, it begins to increase sharply from about 580°C . This signals HE initiation. Figure 3 shows the overall temperature distribution at the moment of initiation. Note the presence of lateral heat conduction. The wind has removed about $250\ \mu\text{m}$ of melt on axis.

Now we consider a range of powers (20–120 kW) on target, along with a range of $1/e$ spot radii (1.8–2.3 cm) at the target. The results for these simulations are summarized in the left-hand plot of Fig. 4. At 120 kW, the initiation times lie between 1.5 and 2.8 s. At 20 kW, the range of initiation times increases to 5.5–8.6 s. As shown in the right-hand plot of Fig. 4, all these times depend not on the power and spot size separately, but rather on the central intensity $I(0)$ via

$$\tau = F_0/I(0) + \tau_0. \quad (2)$$

The least-squares fit parameters are $F_0 = 7.0\ \text{kJ}/\text{cm}^2$ and $\tau_0 = 1.5\ \text{s}$. The fit is best at low intensities, but it is reasonable over the full range.

This behavior can be understood in terms of one-dimensional heat transfer across a material (the metal casing) of width h , with constant material properties. To account for the HE, which is a poor conductor, we impose a zero-conduction boundary condition on the opposite side. The HE initiation time is modeled as the time τ required for the temperature of this side to be raised by an amount T_0 ($\sim 550\text{--}600^\circ\text{C}$ in our case). This problem has an analytic solution,⁵ expressed implicitly in terms of the heat-capacity time $\tau_c = \rho C T_0 h / \alpha I$ (the time to reach a given temperature assuming instantaneous heat conduction) and the

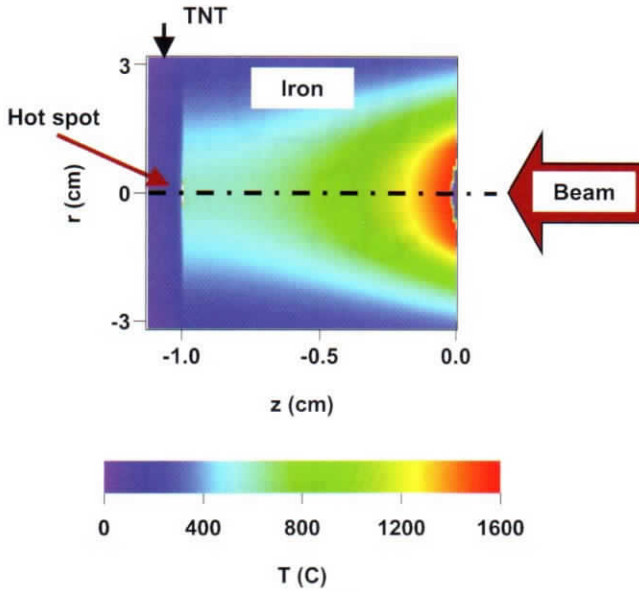


Fig. 3. Temperature distribution in iron and HE, at the moment of HE initiation. The hot spot in the HE (barely visible) is on the beam axis.

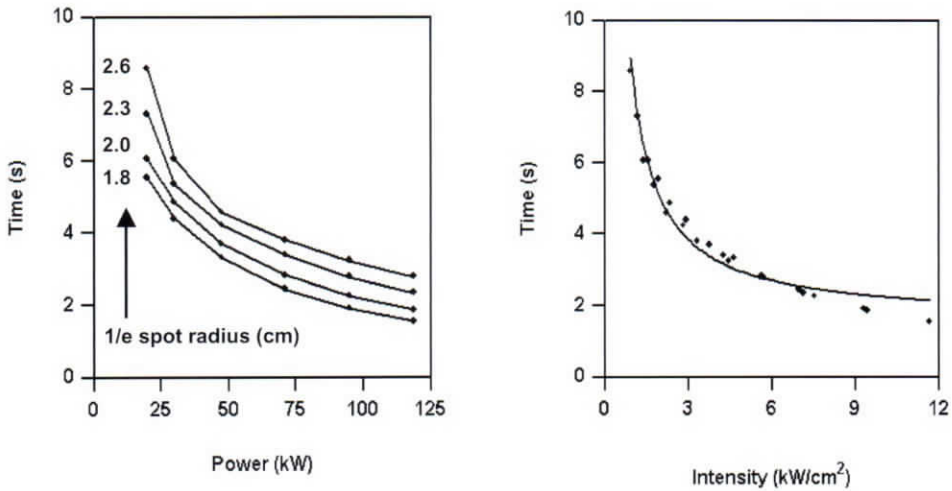


Fig. 4. Left: calculated HE initiation times for a range of powers on target and 1/e spot radii. Right: initiation time versus central intensity. The dots correspond to calculated times, while the solid line gives the fit described in the text.

thermal-conduction time $\tau_D = h^2/D$. Here α is the absorptivity and D is the thermal diffusivity. Expanding the analytic solution in powers of the width, we obtain

$$\begin{aligned} \tau &\approx \tau_C + \tau_D/6 + \dots \\ &= \rho C T_0 h / \alpha I + h^2 / 6D + \dots, \end{aligned} \tag{3}$$

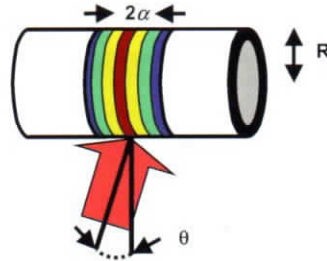


Fig. 5. Schematic deposition of beam energy during rotational averaging.

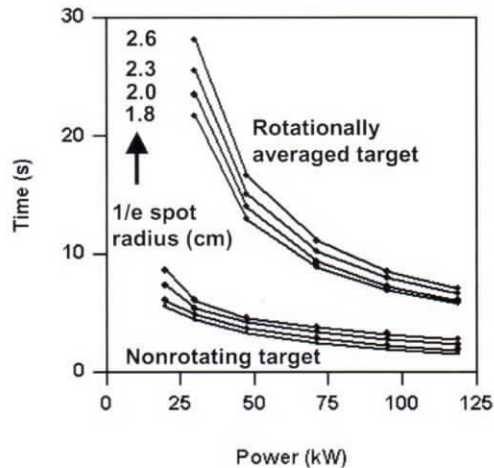


Fig. 6. Calculated initiation times for a rotationally averaged target versus power on the target. The times for a nonrotating target (cf. Fig. 4) are included.

which has the same form as the fit of Eq. (2). In this approximation, therefore, the initiation time involves a weighted sum of the heat-capacity time and the thermal-conductivity time. (Note the factor of $1/6$ multiplying the latter.) This result, with the values given above, is a practical formula for estimating kill times. Since melting is neglected in this simplified treatment, we expect the fit to become less applicable at high intensities, as can be seen in Fig. 4 (right-hand plot).

Now we turn to the rotating case. If the mortar rotates sufficiently rapidly, then the beam energy is deposited uniformly around the circumference of the mortar, as sketched in Fig. 5. In this case, referred to as rotational averaging, the temperature dependence is still two-dimensional, but the coordinates are radial (into the mortar) and parallel to the mortar axis. We assume that rotational averaging is appropriate if two rotations take place during the initiation time, or $\omega\tau \geq 4\pi$. For lower rates of rotation, we interpolate the initiation times between this case and zero rotation. Figure 6 shows calculated kill times for a rotationally averaged mortar. Rotational averaging increases the kill time by a factor ranging from 2.5 to 5.

For a rotationally averaged target, the kill times are fitted by a formula of the same form as for a nonrotating target. In this case, though, the appropriate intensity is the rotationally

averaged central intensity, or $I_{\text{eff}}(0) = P/\pi^{1/2}aC$, where C is the circumference of the target. We find

$$\tau = F_1/I_{\text{eff}}(0) + \tau_1, \quad (4)$$

where $F_1 = 7.4 \text{ kJ/cm}^2$ and $\tau_1 = 1.5 \text{ s}$, equivalent to the parameters in the nonrotating case.

In the cases described up to this point, the laser illuminates the target until the moment of HE initiation (“dwell to kill”). In principle, though, it is possible to stop the laser irradiation before this time and still to achieve HE initiation, as the heat already deposited continues to conduct (“predictive kill”⁹). For our ranges of powers on target and spot sizes, this reduces the rotationally averaged engagement time by about 2.4 s. Even if this is not a deliberate engagement strategy, it allows for a margin of error.

3. Engagement Calculation

A full consideration of practical engagement scenarios would involve a systems analysis. Here we consider a particular scenario, in which a mortar is fired at an asset over a range of 4 km. The asset is protected by a 100-kW SSHCL located at a distance of 1 km, at cross range. The overall geometry and details of the trajectory are indicated in Fig. 7. We assume that the beam director has diameter 30 cm, central obscuration 33%, efficiency 85%, and jitter $2.5 \mu\text{rad}$. It is assumed to be capable of removing beam wander, via tip/tilt control. We assume a beam quality of twice the diffraction limit.

The main processes involved in propagation are diffraction, atmospheric turbulence, absorption, scattering, and thermal blooming. Precise modeling of these effects requires a physical optics code. For our purposes, a less complex treatment is sufficient. We employ

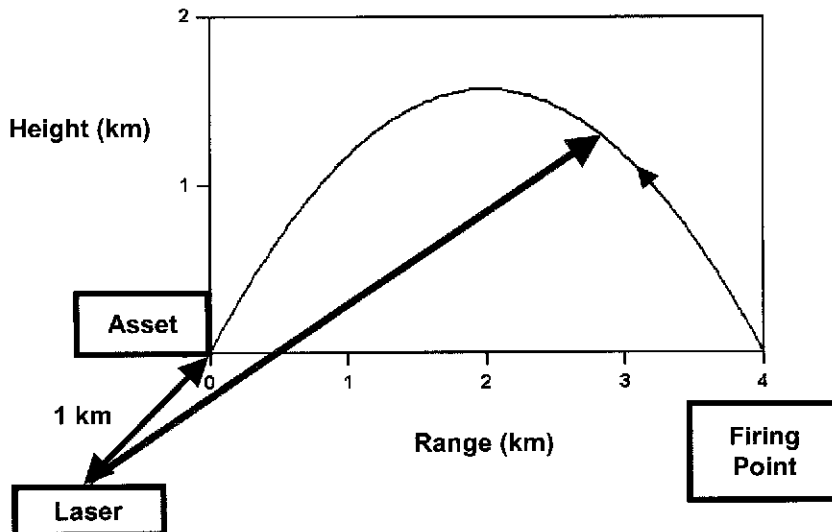


Fig. 7. Engagement scenario considered in this paper. The muzzle speed is 208 m/s, corresponding to two charges. The angle of elevation is about 58 deg, and the time of flight is about 36 s. We assume a frictionless trajectory. The line from the laser to the asset is perpendicular to the plane of the trajectory.

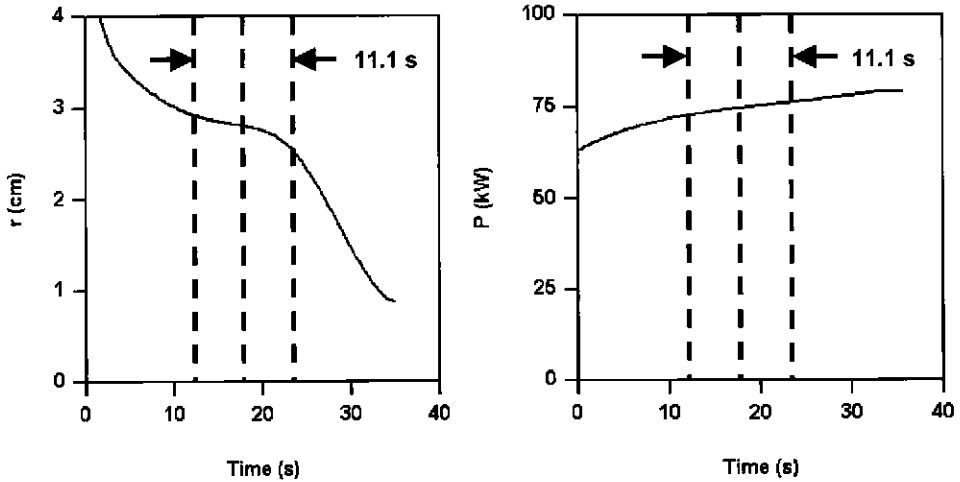


Fig. 8. Left: $1/e$ spot radius on the target during the specific engagement scenario discussed. The kill time for a rotationally averaged target is bracketed. Right: laser power on target.

the BRLPRO propagation code,⁴ which was developed to give rapid, simple propagation results and which has been benchmarked against wave optics treatments. We use this code as driven by NOVAE.⁷ We assume a turbulence level characterized by $C_n^2 = 1 \times 10^{-14} \text{ m}^{-2/3}$ at a height of 10 m, decreasing as $1/h$ with height. The nominal laser height is 2 m. We employ profiles of absorption and scattering coefficients appropriate for midlatitude, summer, rural conditions. For our wavelength, these are due to interactions with aerosols. We consider a visibility of 23 km.

Along the trajectory, the spot size and power on target are calculated as functions of time. The spot is idealized as a Gaussian profile with a particular $1/e$ width. Since the beam generally intercepts the projectile at an angle θ , as illustrated in Fig. 5, the spot area is enhanced by a factor of $1/\cos\theta$. (Thus the effective $1/e$ radius is enhanced by the square root of this factor.) Except near the beginning and end of the trajectory, the spot size is largely determined by diffraction. Turbulent effects are sizable only near the endpoints, due to near-horizontal propagation. Otherwise, they account for only a couple percent of the spot size, as the beam travels substantially upward. Thermal blooming generally accounts for 6% or less.

Figure 8 shows the $1/e$ spot radius and the power on target as functions of time, along the trajectory. Note that these quantities are reasonably flat near the apex, where the mortar is moving most slowly ($\sim 112 \text{ m/s}$). For simplicity, therefore, we assume that the engagement is centered around the apex, with a constant spot radius ($\sim 2.8 \text{ cm}$) and power on target ($\sim 75 \text{ kW}$) appropriate for the apex. The kill time is bounded by the value for a nonrotating mortar ($\sim 4.0 \text{ s}$) and for a rotationally averaged mortar ($\sim 11.1 \text{ s}$). Thus a rotationally averaged situation is obtained at 2 revolutions per 11.1 s, or about 11 rpm. As noted, we interpolate the kill time for lower rotation rates. The peak fluence on target (the kill fluence) ranges from 7.6 kJ/cm^2 (no rotation) to 21.3 kJ/cm^2 (rotationally averaged). It is similarly interpolated.

4. Discussion

Any modeling of countermortar lethality by lasers inevitably neglects some effects. In our case, these would include the following.

1) Target paint was not taken into account. Although paint may survive for some time during the engagement, it tends to increase the absorption.

2) Coupon experiments by our SSHCL group have demonstrated combustion in an iron target,² resulting in an effective increase in absorbed power.

3) The beam was treated as CW, as noted in Sec. 2.

4) The casing was modeled as 10 mm thick. The casing thickness of an actual 82-mm mortar varies with position but is generally less than 10 mm except near the front. Near the rear, it decreases to less than 9 mm.

5) The circumferential curvature of the mortar was not taken into account. This results in a small decrease of absorption near the edge of the spot. But for the large spots under consideration, for which lateral thermal transport is not too important, lethality is determined mainly by the central power. Thus surface curvature effects are not important.

The first four of these effects would lead to increased lethality. As a result, we believe that our lethality estimates are conservative and reliable.

It is interesting that the kill time can be described quite well by the simple formulas of Eqs. (2) and (4), when the intensity is not too high. These can be employed for rapid estimates.

5. Conclusions

We have described a countermortar lethality study, taking into account the complex physics of the laser–target interaction and propagation effects. The kill mechanism is rapid cook-off of the HE. In the sample engagement considered, the kill time ranged from 4.0 to 11.1 s, depending on the mortar rotation rate. It appears that a solid-state heat-capacity laser, operating at 100 kW, can be an effective weapon for countermortar defense.

6. Acknowledgments

This work was supported by the U.S. Army Space and Missile Defense Command. Work was performed under the auspices of the U.S. Department of Energy by the University of California, Lawrence Livermore National Laboratory, under Contract W-7405-ENG-48. We express our indebtedness to R. M. Yamamoto, head of the SSHCL project at LLNL. We also thank R. Snow and G. Edlin for discussions regarding BRLPRO.

References

¹Boley, C.D., and A.M. Rubenchik, "Modeling of Material Removal by Solid State Heat Capacity Lasers," Proc. 15th Annual Solid State and Diode Laser Technology Review, Albuquerque, NM, June 3–6, 2002.

²Boley, C.D., and A.M. Rubenchik, "Modeling of High-Energy Pulsed Laser Interactions with Coupons," University of California, UCRL-ID-151857, Feb. 6, 2003.

³Boley, C.D., and A.M. Rubenchik, "Simulations of Target Interactions with Pulsed, High-Energy Lasers," Proc. 17th Annual Solid State and Diode Laser Technology Review, Albuquerque, NM, June 8–10, 2004.

⁴Breaux, H.J., Proc. SPIE **185**, 192 (1979).

⁵Carlaw, H.S., and J.C. Jaeger, *Conduction of Heat in Solids*, 2nd ed., Clarendon Press (1959).

⁶Frank-Kamenetskii, D.A., Acta Physicochem. USSR **10**, 363 (1939).

⁷Gebhardt, F.G., M.B. Richardson, P. Gillespie, and A.E. Wetmore, "Nonlinear Aerosol Vaporization and Breakdown Effects Module NOVAE," Battlefield Environment Directorate, Army Research Laboratory, White Sands Missile Range, NM, June 1993.

⁸Harrach, R.J., *J. Appl. Phys.* **47**, 2473 (1976).

⁹Kulkarny, V., J. Schwartz, K.C. Moore, Y. Nachshon, and O. Pade, "Short Range Rocket Vulnerability to Laser Radiation," NAUTILUS.018T, TRW Inc., March 27, 1998 (FOUO).

¹⁰LaFortune, K.N., R.L. Hurd, J.M. Brase, and R.M. Yamamoto, Proc. 17th Annual Solid State and Diode Laser Technology Review, Albuquerque, NM, June 8–10, 2004.

¹¹(U) Nugent, J., J. Wilson, J. Schwartz, G. Gerson, and W. Cook, "(U) THIEL Engagement Performance and Model Validation," TRW Space & Defense Space Park, 06615-SP06456-SX-00, May 30, 2002 (unpublished, SNSI).

¹²Soules, T.F., et al., "Ceramic Nd:YAG—Current Material of Choice for SSHCL," Eighth Annual Directed Energy Symposium, Lihue, HI, Nov. 14–18, 2005.

¹³Wenzel, R.F., "Pulsed Laser Lethality Assessment," NRL/MR/6330–02–8619, May 13, 2002 (FOUO).

¹⁴Zinn, J., and C.J. Mader, *J. Appl. Phys.* **31**, 323 (1960).

The Authors

Dr. Charles D. Boley received his S.B. (1966) and Ph.D. (1971) in physics from the Massachusetts Institute of Technology. Since 1986, he has been a physicist at the Lawrence Livermore National Laboratory, where he has modeled phenomena in laser isotope separation, laser materials processing, lasers for inertial fusion (components of the National Ignition Facility, including the plasma-electrode Pockels cell and spatial filter pinholes), and solid-state heat-capacity lasers.

Dr. Alexander M. Rubenchik received his Ph.D. in theoretical physics from the Institute of Nuclear Physics, Novosibirsk, in 1974. He received the Dr.Sci. degree from the Space Research Institute, Moscow, in 1983. Currently, he is a physicist at Lawrence Livermore National Laboratory. His main scientific interests are in the physics of laser–matter interactions, nonlinear optics including studies of optical damage, and plasma physics. He is a member of the DEPS.